The imprint of crustal density heterogeneities on regional seismic wave propagation

Agnieszka Plonka[1], Nienke Blom[1], and Andreas Fichtner[2]

[1]Department of Earth Sciences, Utrecht University, Utrecht, The Netherlands
[2]Department of Earth Sciences, ETH Zurich, Zurich, Switzerland

Correspondence to: a.i.plonka@uu.nl

Abstract. Density heterogeneities are the source of mass transport in the Earth. However, the 3D density structure remains poorly constrained because traveltimes of seismic waves are only weakly sensitive to density. Inspired by recent developments in seismic waveform tomography, we investigate if the visibility of 3D density heterogeneities may be improved by inverting not only traveltimes of specific seismic phases but complete seismograms.

As a first step in this direction, we perform numerical experiments to estimate the effect of 3D crustal density heterogeneities on regional seismic wave propagation. While a finite number of numerical experiments may not capture the full range of possible scenarios, our results still indicate that realistic crustal density variations may lead to traveltime shifts of up to ~ 1 s and amplitude variations of several tens of percent over propagation distances of ~ 1000 km. Both amplitude and traveltime variations increase with increasing epicentral distance and increasing medium complexity, i.e. decreasing correlation length of the heterogeneities. They are practically negligible when the correlation length of the heterogeneities is much larger than the wavelength. However, when the correlation length approaches the wavelength, density-induced waveform perturbations become prominent. Recent regional-scale full-waveform inversions that resolve structure at the scale of a wavelength already reach this regime.

Our numerical experiments suggest that waveform perturbations induced by realistic crustal density variations can be observed in high-quality regional seismic data. While density-induced traveltime differences will often be small, amplitude variations exceeding ± 10 % are comparable to those induced by 3D velocity structure and attenuation. While these results certainly encourage more research on the development of 3D density tomography, they also suggest that current full-waveform inversions that use amplitude information may be biased due to the neglect of 3D variations in density.

1   Introduction

Lateral variations in density are the driving force behind mass transport in the Earth, from crust to core (e.g. Kennett & Bunge, 2008; Turcotte & Schubert, 2014). They are the source of mantle convection, including the ascent of super-plumes and the subduction of lithospheric plates. Knowledge of density is essential to discriminate between compositional and thermal heterogeneities (e.g. Trampert *et al.*, 2004; Mosca *et al.*, 2012), infer the nature of continental lithosphere (e.g. Jordan, 1975, 1978) or understand the relation between mantle convection and surface tectonics (e.g. Bunge *et al.*, 2003; Liu & Gurnis, 2008;

Warners-Ruckstuhl *et al.*, 2012). Despite its outstanding importance for the solid-Earth sciences, the 3D density structure of our planet remains poorly constrained.

1.1 The (in-)sensitivity of seismic data to 3D density variations

Unlike seismic velocities that can be inferred from the travel times of elastic waves, unambiguous information on density is difficult to find in most seismic observables.

Within the framework of seismic ray theory (e.g. Cerveny, 2001), seismic traveltimes are exactly insensitive to density variations. In finite-frequency theory, the sensitivity of body waves to density is non-zero, but mostly confined to the immediate vicinity of sources and receivers (e.g. Tromp *et al.*, 2005; Fichtner, 2010). The physical origin of this nearly complete absence of sensitivity lies in the scattering characteristics of density heterogeneities. When a body wave reaches a density perturbation, the resulting scattered wave propagates backwards, meaning that it cannot interfere with the incident wave unless the heterogeneity is located within one wavelength from either source or receiver (Wu & Aki, 1985; Tarantola, 1986; Trampert & Fichtner, 2013). This is in contrast to the scattered wave caused by a velocity heterogeneity, which propagates along with the incident wave, thereby leading to a finite-frequency traveltime shift (e.g. Tong *et al.*, 1998; Marquering *et al.*, 1999; Dahlen *et al.*, 2000). Since scattered waves caused by density heterogeneities must exist, one may conclude that seismograms in general are sensitive to density variations, but this information cannot be contained in direct body wave traveltimes.

Unlike body wave traveltimes, the frequency-dependent traveltimes of Rayleigh waves reveal significant non-zero sensitivity to density variations (e.g. Takeuchi & Saito, 1972; Aki & Richards, 2002). The origin of this sensitivity can be understood intuitively with the mode-ray duality. Rayleigh waves can be seen as constructively interfering P-SV waves that reflect multiple times off the free surface. The reflection coefficient depends on density in the vicinity of the surface, thereby affecting the dispersion properties of the interference pattern. Unfortunately, Rayleigh wave sensitivity to density is strongly oscillatory, which leads to cancellation effects that leave little effective sensitivity to larger-scale variations.

At the long-period end of the seismic spectrum, the gravest normal modes of the Earth are sensitive to long-wavelength density structure as a result of the gravitational restoring force (Woodhouse, 1988; Dahlen & Tromp, 1998; Woodhouse & Deuss, 2007). This may be used to constrain density variations in the lower mantle where low-degree structure is known to be dominant (e.g. Dziewoński *et al.*, 1977; Becker & Boschi, 2002).

1.2 Previous work and possible future directions

Despite these difficulties, various attempts have been made to constrain 3D density structure in the Earth. On the global scale, geodynamic data, including estimates of plate motion history and the location of subducting slabs, may be used to constrain the broad distribution of density in the mantle (Richards & Lithgow-Bertelloni, 1993; Nataf & Ricard, 1996; Simmons *et al.*, 2010). Seismic constraints on 3D density variations in the lower mantle were first presented by Ishii & Tromp (1999, 2001, 2004) based on long-period normal-mode measurements. The robustness of their results has, however, been questioned by various authors (e.g. Resovsky & Ritzwoller, 1999; Romanowicz, 2001; Kuo & Romanowicz, 2002; Resovsky & Trampert,

2002). Recently, Koelemeijer *et al.* (2015) have shown that density estimates from previously used normal-mode data are not robust. However, with the incorporation of the latest data, these inferences can be improved significantly.

On regional scales, several authors jointly inverted body wave traveltimes and gravity data under the assumption seismic velocities and density are almost uniformly scaled to each other (e.g. Tondi *et al.*, 2000, 2009; Maceira & Ammon, 2009). While being correct for purely thermal density variations, this assumption prevents the detection of those interesting cases where velocities and density are not simply scaled due to the presence of compositional heterogeneities.

With the steadily increasing quality of seismic data, new observables with sensitivity to 3D density variations are becoming sufficiently robust. Lin *et al.* (2012); Lin & Tsai (2012) propose to use Rayleigh-wave ellipticity and local amplification measurements to estimate lithospheric density variations. The design of seismic observables with maximum sensitivity to density and minimum trade-offs to other parameters, e.g. velocities, has been suggested by Bernauer *et al.* (2014).

In addition to improving data quality, new opportunities may arise from the development of full-waveform inversion techniques that are capable of exploiting complete seismograms without being restricted to the well-known seismic phases (e.g. Chen *et al.*, 2007; Fichtner *et al.*, 2009; Tape *et al.*, 2010; Fichtner *et al.*, 2013). As shown by Rickers *et al.* (2012, 2013), the exploitation of scattered waves in full-waveform inversion can lead to substantial improvements in regional 3D velocity images. However, the potential of full-waveform inversion to better constrain density variations in the crust and upper mantle remains largely unexplored.

1.3 Outline

As a first step towards full-waveform inversion for regional density structure, we present a study on the imprint of 3D density heterogeneities in the crust on seismic wave propagation in the period range from 8 - 50 s. For this, we conduct a series of numerical experiments, where we analyse seismic wave propagation through random Earth models with variable complexity, i.e. correlation length scale. These models are designed to represent ~~are~~ a range of plausible 3D heterogeneous crustal environments. While wave propagation through random media has been widely used to quantify the effect of velocity heterogeneities (e.g. Frankel & Clayton, 1986; Frankel, 1989; Igel & Gudmundsson, 1997; Furumura & Kennett, 2005; Kennett & Furumura, 2008; Meschede & Romanowicz, 2015), variations in density have so far not been considered. Our experiments are intended to (i) provide rough estimates of the amplitude and traveltime variations related to realistic density variations, and (ii) better understand the physics behind density-induced waveform perturbations.

Following a presentation of the numerical setup, we will present detailed analyses of traveltime and amplitude variations induced by 3D crustal density heterogeneities. We expect scattering to be the dominant mechanism by which density heterogeneities influence the seismic signal. Scattering is most effective when scatterers are of similar size or smaller than the wavelength, which is why we will study the influence of frequency, propagation distance and medium complexity. Being focused on a future full-waveform inversion for density, we do not consider specific seismic phases, but try to provide ensemble estimates of waveform perturbations. Given the complexity of regional-scale seismic waveforms at periods below ~ 20 s, it is

clear that this analysis can never be complete and exhaustive. It will, however, provide a first crude estimate of the impact of crustal density structure on seismic wave propagation.

2 Setup of the numerical experiments

2.1 Numerical wave propagation

5 To assess the impact of 3D density heterogeneities in the crust on seismic wave propagation, we compute numerical solutions to the elastic wave equation (e.g. Kennett, 2001; Aki & Richards, 2002)

$$\rho(\mathbf{x})\,\partial_t^2 u_i(\mathbf{x},t) - \partial_j[c_{ijkl}(\mathbf{x},t) * \partial_k u_l(\mathbf{x},t)] = f_i(\mathbf{x},t)\,, \tag{1}$$

which relates mass density ρ, the elastic tensor c_{ijkl}, and an external force f_i to the displacement field u_i. With our focus being on regional wave propagation at periods below 50 s, we can safely ignore the Earth's rotation and self-gravitation. Furthermore, 10 we restrict ourselves to an isotropic rheology.

For the numerical solution of equation (1), we employ the spectral-element solver SES3D (Fichtner *et al.*, 2009; Gokhberg & Fichtner, 2016). The spectral-element method, widely used in seismological research, allows us to compute accurate numerical solutions in the presence of strong 3D heterogeneities, and without requiring special treatment of the free surface ~~(e.g. Faccioli *et al.*, 1996; Komatitsch & Vilotte, 1998; Komatitsch & Tromp, 1999; Peter *et al.*, 2011)~~ (e.g. Faccioli *et al.*, 1996; Komatits

15 Our computational domain is a spherical section that is ~ 2000 by ~ 1000 km wide and 500 km deep. As background model we use the radially symmetric Preliminary Reference Earth Model (Dziewoński & Anderson, 1981), where we replace the original 24 km thick crust by a 40 km thick crust that better represents continental structure.

Since the number of receivers has no significant impact on the computational costs of the numerical simulations, we use a dense grid of 930 receivers, distributed evenly across the surface of the computational domain. In the wavefield simulations, 20 we calculate 700 s long velocity seismograms from a strike-slip source. The complete setup is shown in figure 1.

2.2 Random media generation

With the true 3D density structure of the crust being insufficiently constrained, we use synthetic random density models in our numerical wave propagation experiments. For this, we superimpose random velocity and density variations with pre-defined correlation lengths in the horizontal and vertical directions onto the crustal part of the background model, i.e. the upper 40 25 km. The spatial variations in velocity and density are statistically uncorrelated~~.~~, meaning that the spatial correlation averaged over many realisations is negligibly small. Individual realisations, considered in this work, do have non-zero correlation. In Appendix A, we summarise the computation of 3D random models based on the widely-used Fourier method.

To ensure that the amplitudes of velocity and density variations are realistic, we combine information from tomographic models and empirical velocity-density scalings. For this, we compute the root-mean square (rms) of the S velocity variations in the

regional crustal model of Anatolia obtained by Fichtner *et al.* (2013) using full-waveform inversion. S velocities at crustal depths in this model are resolved on length scales of ∼ 25 km. Using the empirical scaling relations between crustal velocities and density of Brocher (2005), we then obtain suitable ranges for variations in P velocity and density. The resulting rms variations are 260 m/s for S velocity, 460 m/s for P velocity, and 80 kg/m^3 for density. Two particular realisations of random density variations with different correlation lengths are shown in figure 2. While the random models are intended to represent plausible variations of crustal structure, there exists of course uncertainty related to the poorly known amplitude spectrum of these variations in the real Earth, and the range of different velocity-density scalings proposed in the literature. We discuss these issues in more detail in section 4.2. We note that random velocity and density models used in our simulations are on purpose spatially uncorrelated. Empirical velocity-density scalings are used only to determine plausible rms variations.

2.3 Quantification of waveform differences

In our numerical experiments, we use media with homogeneous crustal density and random 3D variations in P and S velocities as reference. We then compare synthetic seismograms from the reference medium with synthetic seismograms from a medium where random variations in density are added.

Since our ultimate goal is to use complete three-component seismograms to constrain density in the Earth, we do not compare isolated and well-defined seismic phases. Instead, we compute time- and frequency-dependent traveltime and amplitude differences. For this, we bandpass filter the seismograms into a pre-defined frequency band and apply a zero-centred moving window $w(t)$ that transforms a component of a seismogram $u(t)$ into its windowed version $\hat{u}_\tau(t) = w(t - \tau)u(t)$. The traveltime difference δT as a function of τ is then defined as the argument of the maximum of the cross-correlation:

$$\delta T(\tau) = \underset{t}{\text{argmax}\,\text{argmax}} \int \hat{u}_\tau^{\text{ref}}(t')\hat{u}_\tau(t + t')dt', \tag{2}$$

where $\hat{u}_\tau^{\text{ref}}$ denotes the windowed seismogram for the reference medium with homogeneous crustal density. In the case of $\delta T < 0$, the wave for 3D heterogeneous density arrives earlier than the reference wave, and vice versa. Similarly, we measure relative amplitude variations δA as a function of time:

$$\delta A(\tau) = \frac{\sqrt{\int [\hat{u}_\tau(t)]^2\, dt} - \sqrt{\int [\hat{u}_\tau^{\text{ref}}(t)]^2\, dt}}{\sqrt{\int [\hat{u}_\tau^{\text{ref}}(t)]^2\, dt}} \tag{3}$$

In the following sections, we consider three frequency bands of variable width: 0.02 - 0.125 Hz (8 - 50 s), 0.02 - 0.067 Hz (15 - 50 s), and 0.02 - 0.04 Hz (25 - 50 s). The $w(t)$ Gaussian time windows corresponding to those frequency bands have standard deviations of 8 s, 15 s and 25 s, respectively. To stabilise the measurements, we exclude those parts of the synthetic seismograms where the average amplitude within a time window is below 5 % of the maximum within the complete trace.

While more information-rich quantifications of seismic waveform differences may be constructed, for instance on the basis of wavelet transforms (e.g. Kristekova *et al.*, 2006, 2009), we prefer the traveltime and amplitude differences defined in equations (2) and (3) for their robustness and ease of interpretation. Similar quantifiers of waveform differences are frequently used in

full-waveform inversion (e.g. Fichtner *et al.*, 2008; van Leeuwen & Mulder, 2010; Bozdağ *et al.*, 2011; Rickers *et al.*, 2012, 2013).

Since density impacts P and S energies in the same way, there is no need for any component rotation.

3   Impact of density heterogeneities on wave propagation

In the following sections, we present a phenomenological study on the impact of crustal density heterogeneities for media with different horizontal and vertical correlation lengths, summarised in table 1. For each experiment, we compare three-component seismograms in three different frequency bands: seismograms computed for a medium with 3D random density variations are compared with seismograms for the reference medium with homogeneous crustal density. We specifically analyse the effects of frequency (section 3.2), epicentral distance (section 3.3), and medium complexity (section 3.4). Here and in the following sections, we use 'increasing complexity' as synonymous to 'decreasing correlation length'.

3.1   A single-receiver example

We start with the analysis of media with 200 km lateral and 20 km vertical correlation length. This will serve as a baseline for later simulations with models that have either more or less complexity. ~~Figure 3 shows a comparison of three-component seismograms for homogeneous and heterogeneous crustal densities in the broadest frequency band from 0.020 - 0.125 Hz (8 - 50 s).~~ Before attempting a more comprehensive analysis in the following sections, we consider a single receiver located at 910 km epicentral distance, marked by the red triangle in figure 1. Figure 3 shows a comparison of three-component seismograms for homogeneous and heterogeneous crustal densities in the broadest frequency band from 0.020 - 0.125 Hz (8 - 50 s).

Waveform differences mostly tend to increase with increasing traveltime, in accord with the expectation that (multiply) scattered waves should arrive later than the primary waves by which they have been excited. The magnitude of the time shifts are approximately independent of the component, reaching around 0.5 s. Relative amplitude differences are largest on the E-W and vertical components, where the displacement velocity itself is smallest ~~so that the influence of scattered waves is largest~~. Therefore, low-amplitude scattered waves have the largest influence on the total amplitude. They regularly exceed 50 % in both directions, meaning that amplitudes for the heterogeneous density crust can be ~~both twice and~~ either twice or half as large as for the medium with homogeneous crustal density. On the N-S component, where the displacement velocity is largest, relative amplitude differences vary between ± 10 %.

Figure 4 displays time shifts and relative amplitude differences for five different realisations of random media, at the same receiver and for a lower frequency band from 0.02 - 0.04 Hz. Both traveltime and amplitude variations differ significantly for different media, which has two important implications: (i) Different media may be distinguished from each other, at least to some extent that remains to be quantified. (ii) To obtain statistically significant results in the present study, we must average traveltime and amplitude variations over various random realisations. Based on our experience, five realisations are sufficient

to obtain reliable results.

In addition to the dependence on the random velocity and density structure, figure 4 also reveals that the waveform differences in the lower frequency band from 0.02 - 0.04 Hz are on average smaller than for the higher frequency band from 0.020 - 0.125 Hz. In the following section, we will investigate this frequency dependence in more detail.

3.2   The effect of frequency

A variant of figure 3 for the narrower and lower frequency band from 0.02 - 0.04 Hz (25 - 50 s) is shown in figure 5. While relative amplitude differences are markedly smaller than at higher frequencies, the traveltime differences are still comparable.

This preliminary, and mostly visual, analysis of frequency dependence indicates that waveform differences are primarily caused by scattering that transfers energy from the large-amplitude N-S component onto the smaller-amplitude E-W and vertical components. Constructive and destructive interference between primary and scattered waves may cause the wave amplitudes to deviate in both directions. An increase of amplitudes may be further supported by additional wave focusing induced by 3D density heterogeneities. The approximate frequency independence of traveltime differences, however, can hardly be explained with basic wave propagation intuition.

To make our analysis more comprehensive and efficient, we compute histograms of time shifts and relative amplitude differences for all 930 stations in the receiver grid. In line with our future goal, which is to use full-waveform inversion to constrain 3D density variations, we do not consider specific seismic phases, but longer time series that comprise body, surface and scattered waves. ~~For this, we perform measurements in a~~ After calculating the misfits for all of the receivers of the grid, we stack their values into histograms, each histogram corresponding to a different frequency band. The values that we consider in the stacking procedure are measured up to 300 s ~~long time interval, starting at the P wave arrival. This procedure ensuresthat~~ after the first difference between the two waveforms (shortly after the first arrival of the P wave). This ensures, firstly, that the difference in epicentral distance between receivers does not affect the histogram shape, and secondly, that most of the waveforms with large enough amplitudes are included, while excluding low-amplitude parts of the seismograms where numerical errors have a larger impact. In order to obtain representative results, we average the measurements of time shift and relative amplitude differences over five random media realisations. Histograms showing the effect of bandwidth on time shifts and relative amplitude differences are displayed in figure 6.

Relative amplitude differences for the broader frequency band, i.e. for frequencies that are on average higher, have a considerably larger spread than at lower frequencies. In the 0.02 - 0.125 Hz band, the standard deviation of the amplitude differences is 0.15. Amplitudes can be both smaller and larger than in the reference scenario with homogeneous crustal density. Within the lower frequency band from 0.02 - 0.04 Hz, the standard deviation of the amplitude differences is reduced to 0.07, suggesting that the single-station analysis from figures 3 and 5 has more general validity.

The dependence of time shifts on frequency is more complex, as shown in the left panel of figure 6 and in table 2. The standard deviation reaches 0.2 s for the two highest frequency bands (0.02 - 0.125 Hz and 0.02 - 0.067 Hz), and surprisingly increases

to 0.38 s for the lowermost frequency band from 0.02 - 0.04 Hz.

To investigate this phenomenon further, we show histograms for the lowest and highest frequency bands for a single random medium realisation and for the three different components in the top row of figure 7. We observe a distinct tail of reduced time shifts of ~ 1 s on the E-W component and for the lowest frequency band. A similar observation can be made for two out of five random media, suggesting that these time shifts are not highly unlikely to be artefacts of an unusual random medium realisation. The bottom row of figure 7 shows a pair of synthetic seismograms at an epicentral distance of ~ 1300 km that contributes to this tail of negative time shifts . In the in the mentioned histograms - we show directly by plotting this exemplary pair that in the lower frequency band (from 0.02 - 0.04 Hz~~waves~~) the waveforms for the 3D heterogeneous crust arrive early by ~ 1 s. ~~Histograms for larger epicentral distance have much bigger spread, and the isolated tail of negatve timeshifts~~ The tail of negative time shifts appears only for ~~far away stations~~ stations of distance between 1000 km and 1200 km (the far away stations) and is absent for stations of epicentral distance between 100 km and 300 km (the stations close to the source). We examined this distance dependence further, using synthetic data from one of the numerical experiments contributing to the tail~~, and found that for~~ . For all the frequency bands for ~~stations of epicentral distance between 1000 and 1200 km~~ far away stations, the mean time shift value is shifted to negative values between -0.08 and -0.14 s. While the mean time shift ~~value is~~ values are similar for all the frequencies in question, the standard deviation of time shift for the lowest frequency band is three times as big as for the other bands and reaches 0.8 s. We do not observe any of those relations for ~~stations of epicentral distance between 100 and 300 km~~ the stations close to the source. A visual waveform comparison suggests that the traveltime differences may be a finite-frequency effect, meaning that waveform (amplitude) differences within short time intervals translate into time shifts when these are measured by cross-correlation within a finite frequency band. We discuss this aspect in more detail in section 4.1.

3.3 The effect of epicentral distance

To investigate whether density-related traveltime and amplitude differences are only local effects or accumulate with propagation distance, we plot histograms for stations in two different epicentral distance ranges: 100 - 300 km and 1000 - 1200 km. We again average over five random media realisations with 200 km lateral and 20 km vertical correlation length. The results for the broadest frequency band from 0.02 - 0.125 Hz are shown in figure 8.

For epicentral distances between 100 – and 300 km, the variance of the time shifts is 0.15 s, and it increases to 0.64 for epicentral distances between 1000 – and 1200 km. Similarly, the variance of relative amplitude differences increases from 0.007 to 0.111. This indicates that waveform differences due to crustal density heterogeneities indeed accumulate with increasing epicentral distance, which is an essential prerequisite for the use of tomographic methods.

3.4 The effect of medium complexity

In order to reveal the physical origin of the waveform differences, we consider random media with different lateral correlation lengths, listed in table 1. We again work with the broadest frequency band from 0.02 - 0.125 Hz.

As shown in the top row of figure 9, the medium with 50 km lateral correlation length leads to a broad distribution of time shifts and relative amplitude differences, compared to the medium with 200 km lateral correlation used in the previous sections. The standard deviations of time shifts and relative amplitude differences reach values of 0.94 s and 0.20, respectively. In contrast, traveltime and amplitude variations for the smooth medium, shown in the bottom row of figure 9, are nearly zero for all times and for all receivers. Their standard deviations are 0.01 s and 0.01, respectively.

The histograms in figure 9 indicate that waveform differences induced by 3D density variations occur mostly due to scattering which is most effective when heterogeneities are equal or smaller in size than the wavelength. In a medium with 50 km lateral correlation length, the size of heterogeneities is comparable to the wavelength of waves with a maximum frequency of 0.125 Hz, and scattering becomes the dominant mechanism to perturb the wavefield. In the smooth medium with 1000 km lateral correlation length, the dominant mechanism is transmission, which clearly has no significant impact on either traveltimes or amplitudes.

4   Discussion

4.1   Seismic signatures of crustal density heterogeneities

Our numerical experiments show that 3D crustal density heterogeneities may lead to both positive and negative variations in the traveltimes and amplitudes of seismic waves. This indicates that 3D density structure leaves an imprint on regional seismic wavefields that goes beyond simple scattering attenuation of the main arrivals.

To understand the effects which play a major role in wave propagation, we look first at the misfit histograms for different frequency bands (section 3.2). Intuitively, the histogram for the frequency band in which more misfits are accumulated should have smaller zero peak and bigger spread. We would expect to observe more misfits for higher frequencies due to illumination of finer structures. However, as can be seen in figure 6, while the peak around zero is smaller for the lower frequency band for both time shifts and amplitude differences, the spread is comparable for time shifts and larger for the higher frequency band for amplitude differences. This may mean that we observe ~~two separate effects affecting wave propagation that~~ a variety of effects that affect wave propagation and have different impact on the observed seismograms for different frequency bands. ~~One of those noticeable effects could be that , with~~ Below we discuss this seemingly counterintuitive result.

Our lowest bandwidth has a peak frequency of 0.03 Hz, which translates into a dominant wavelength of roughly 100 km for a wave travelling with the velocity of $3.2 \frac{km}{s}$ (the PREM value for crustal S velocity). Since the lateral cross-correlation length of the random medium used in our setup is 200 km, the lateral mean size of a scatterer should reach the value of around 100 km, which matches the dominant wavelength of the lowest bandwidth. This would mean that in this bandwidth, we will observe resonant scattering for waves travelling horizontally with the velocity of around $3.2 \frac{km}{s}$. In consequence, due to more scattering, we will measure higher values of density-related misfits. Increasing the peak frequency to 0.07 Hz, which is the peak frequency of our highest bandwidth $(0.02 - 0.125$ Hz), would decrease the dominant wavelength for an S wave to around 50 km, and thus

move us away from resonance. In that case, with increasing frequency, scattering off heterogeneities becomes less significant in favour of transmission effects. That essentially means approaching the range of the infinite-bandwidth approximation of ray theory validity, in which we completely lose sensitivity to density. Smaller scattering in higher frequencies may mean that we will observe more misfits of values around zero, causing the histograms for the higher frequency band to have larger zero peaks.

An increase of the peak frequency of the bandwidth in our particular case means observing less scattering for certain waves, however, it also means a proportional increase in relative propagation distance. This implies that we will observe waveform differences accumulated for bigger number of wavelenghts, and the amount of large non-zero density related misfits will increase. This is an effect that changes the histogram shape in a way opposite to moving away from resonance. The larger propagation distance could be then one of the reasons behind the broader histogram spread for the higher frequency band.

Increasing the relative propagation distance is equivalent to moving further from the source, which is consistent with section 3.3, where we show that density-related misfits accumulate with distance. The observation of more waveform differences with larger epicentral distance also suggests that the impact of density structure is not merely a local effect, but rather an integral over the complete wavepath - an essential prerequisite for performing tomography.

While the results for different frequency bands are physically governed by the amount of scattering and the length of the relative propagation distance, and the results for different epicentral distances by the length of the propagation distance only, for various medium complexities we observe how important scattering is for sensitivity to density. The noticeable change in histogram shape in figure 9 is caused by much bigger amount of scattering for more complex media. Especially the nearly complete absence of waveform differences for long-wavelength density heterogeneities indicates that the scattering is the dominant mechanism to produce these waveform differences. The energy transfer between the different components and towards later arrivals is also scattering-related.

As we show, the behaviour of density-induced misfits can be most often explained by an interplay of two physical parameters: the amount of scattering and the relative propagation distance. However, not all of the observed features can be interpreted on this ground. For instance, traveltime variations do not seem to exhibit a pronounced frequency-dependence, in contrast to amplitude variations that decay rapidly with decreasing frequency (see section 3.2 and figure 6). Since the traveltimes of seismic waves are exactly independent of density in the infinite-bandwidth approximation of ray theory (Cerveny, 2001), the traveltime differences observed in our experiments are most likely due to finite-frequency effects. Traveltime differences measured by cross-correlation within a finite frequency band are controlled by the complex interference of direct and scattered waves, which may lead to seemingly paradoxical effects (e.g. Tong *et al.*, 1998; Marquering *et al.*, 1999; Dahlen *et al.*, 2000). This may include the large negative traveltime differences shown in figure 7.

Figure 10 illustrates finite-frequency traveltime changes for a 2D P-SV wavefield simulation. While interacting with a density anomaly, the wavefield undergoes reflections and amplitude changes. The actual onset time of the wavefront remains largely unaffected. However, the waveform differences translate into a cross-correlation traveltime shift of ~ 1 s.

We should also take into account the possible signal processing artefacts that may play a role in our analysis. In comparing between different frequency bands, we are effectively changing the bandwidth used. Therefore, some of the large time shifts that are visible in the lower frequency histogram in figure 6 could be a result of the existence of non-zero cross-correlation maxima for a narrow bandwidth, which would be purely signal-processing related and have no physical interpretation. We do not expect to observe this effect in the broader frequency bands.

Naturally, scattering is a complex process that depends on the ratio of the scatterer size to the wavelength, the strength of scatterers and the source power (Groenenboom and Sneider, 1995). The signal processing artefacts and physical scattering signatures are not easily separated. Investigating whether the misfits accumulate later in the coda, which would indicate that they are scattering-related, and determining an optimal processing bandwidth size in order to decrease the amount of artificial large cross-correlation maxima, could be favorable future steps.

The density-induced waveform differences that we found in our numerical experiments are above the noise level of many of today's regional-scale seismic recordings. While this indicates that density heterogeneities do leave a measurable imprint, it does not automatically imply that crustal density structure can be easily recovered in a tomographic inversion. Trade-offs with P and S velocity structure, for instance, may prevent the unambiguous reconstruction of density heterogeneities. The resolvability of density structure may be analysed using principal-component analysis of finite-frequency kernels (Sieminski *et al.*, 2009), and it may be improved by the construction of targeted misfit functionals (Backus & Gilbert, 1968, 1970; Bernauer *et al.*, 2014).

Finally, we note that the amplitude of the secondary wavefield scattered off density heterogeneities may have similar or smaller amplitudes than globally propagating waves, e.g. PcP, PcS or ScS. Therefore, care needs to be taken when wave propagation is modelled regionally (e.g. Cupillard et al., 2012; Gokhberg & Fichtner, 2016).

4.2 Random models of plausible Earth structure

In the absence of detailed information on crustal density structure on regional scales, we base our numerical experiments on realisations of random Earth models. To ensure that the random models are plausible, we translate rms variations in S velocity in the Anatolia model of Fichtner *et al.* (2013) into variations of P velocity and density, using the empirical velocity-density scaling of Brocher (2005). The plausibility of the random models is limited by three factors: (i) the variability of regional-scale rms variations in S velocity, (ii) the poorly known amplitude spectrum of velocity and density variations in the crust, and (iii) the range of different velocity-density scalings proposed in the literature.

The rms variations in S velocity in the Anatolian crust are ~ 260 m/s, with a horizontal correlation length of ~ 200 km and a vertical correlation length of ~ 20 km. These correlation lengths were used for most of the numerical experiments, except for those in section 3.4, where we studied the effect of medium complexity. Similar S velocity variations on the order of ± 10 % over similar distances were found in tomographic studies of other regions, including the Iberian Peninsula (e.g. El Moudnib

5 *et al.*, 2015; Fichtner & Villaseñor, 2015), California (e.g. Shapiro *et al.*, 2005; Tape *et al.*, 2010), the Caribbean plate (e.g. Gaite *et al.*, 2015), or East Asia (e.g. Chen *et al.*, 2015). This suggests that the rms variations of S velocity variations with 200 km lateral and 20 km vertical correlation length are representative of real crustal structure at least in some regions.

For simplicity, we assume that the amplitude spectrum of the crustal velocity variations is white, meaning that velocity and density variations have nearly identical power at all scales considered in this study, i.e. from 50 - 1000 km. The resulting

10 velocity and density variations may be too large or too small by several percent, depending on whether a specific region is long-term stable and subject to recent tectonic activity.

Uncertainties in velocity-density scalings are mostly caused by the natural scatter of the velocity-density relation in natural rocks. While S velocity typically varies less than ~ 10 % for a given crustal P velocity, density can easily vary by more than 50 % for a given v_P/v_S ratio (Brocher, 2005). Despite the natural scatter, published velocity-density relationships for the

15 continental crust as a whole show good agreement with their respective range of validity (e.g. Ludwig *et al.*, 1970; Gardner *et al.*, 1974; Christensen & Mooney, 1995), suggesting that the choice of a particular one does not introduce a significant bias.

In the light of these uncertainties, it must be kept in mind that the waveform variations resulting from our synthetic random density heterogeneities represent a first rough estimate. It is intended to reveal the first-order effects but not the smaller details that certainly depend on the characteristics of a specific region.

20 ## 4.3 Velocity bias estimation

The shifts in travel time observed here as a result of density structure may cause a bias in velocity structure obtained in tomographic models. In order to obtain an estimate of these velocity biases, we take a simplified approach. We consider the highest frequency band from 0.02 - 0.125 Hz and the reference medium with 200 km lateral and 20 km vertical correlation length, previously used in section 3.3 on the effect of epicentral distance. Since we do not analyse specific seismic phases,

25 we take the time shift variances for different epicentral distances as representative values of time shifts induced by 3D density structure. Furthermore, we assume that sensitivity to velocity structure is concentrated on the great circle connecting source and receiver.

Based on these simplifications, we estimate that the shear velocity bias for an epicentral distance of 200 km is ~ 25 m/s or ~ 0.78 % relative to the upper-crustal shear velocity of PREM (Dziewoński & Anderson, 1981). For epicentral distances of

30 1000 km, the same bias is ~ 21 m/s or ~ 0.66 %. It follows that the velocity biases induced by the neglect of 3D density variations are small compared to the crustal velocity variations inferred from traveltime tomography, which are on the order of 10 %. However, depending on the tomographic resolution and data quality, the biases may be larger than the error bars. A

qualitative look at the detrimental effects that incorrect density information has on the wave speed models has recently been shown by Yanhua O Yuan and Bozdag (2015) .

4.4 Attenuation bias estimation

To quantify potential biases in attenuation induced by unknown 3D density structure, we adopt similar simplifications as in
5   the previous section. In the ray theory approximation, relative amplitude differences between attenuated and attenuation-free waves are given by

$$A = e^{\frac{-\pi r f q}{v}} , \tag{4}$$

with the background attenuation or inverse quality factor denoted by q, the epicentral distance by r, frequency by f, and velocity by v. The presence of 3D density heterogeneity induces additional relative amplitude differences, δA, that translate
10   into apparent variations in attenuation δq,

$$A + \delta A = e^{\frac{-\pi r f (q + \delta q)}{v}} . \tag{5}$$

Combining equations (4) and (5), yields the fractional apparent attenuation bias $\delta \ln q$ as a function of δA,

$$\delta \ln q = \left[\frac{\ln(A + \delta A + 1)}{\ln(A + 1)} - 1 \right] . \tag{6}$$

Equation (6) reveals that attenuation biases for a given δA have a dependence on the background attenuation q through $A =$
15   $e^{\frac{-\pi r f q}{v}}$. The bias is larger for larger attenuation. Figure 11 shows fractional attenuation biases $\delta \ln q$ as a function of the background attenuation q for an epicentral distance of 1000 km, the highest frequency band from 0.02 - 0.125 Hz, and the medium with 200 km lateral and 20 km vertical correlation length. Amplitude variations for this setup are summarised in the right panel of figure 8.

Taking the variance of the relative amplitude differences of 0.11 as a representative value (see section 3.3), the apparent
20   variations in attenuation, $\delta \ln q$, approximately range between ± 20 % and ± 60 % for q between 0.001 and 0.010 (Q between 100 and 1000). It follows that the apparent variations in attenuation induced by 3D density structure can be on the order of tens of percent, thus being comparable to attenuation heterogeneities found on regional and global scales (e.g. Mitchell, 1995; Romanowicz, 1995; Haberland & Rietbrock, 2001; Selby & Woodhouse, 2002; Dalton *et al.*, 2008; Kennett & Abdullah, 2011; Trampert & Fichtner, 2013; Zhu *et al.*, 2015). This result highlights that 3D density structure should be taken into account when
25   using full-waveform techniques to invert for 3D variations in attenuation.

5   Conclusions

We presented a series of numerical experiments to study the effect of 3D crustal density heterogeneities on regional seismic wave propagation in the frequency range from 0.02 - 0.125 Hz (8 - 50 s). These were intended to (i) reveal the extent to which density-induced waveform perturbation may be measurable, and (ii) facilitate a better intuitive understanding of the underlying

wave propagation physics.

While numerical experiments can of course never be exhaustive, our series of tests still allows us to make a limited number of general statements: For media with 200 km lateral correlation length, traveltime perturbations can exceed ~ 1 s over an epicentral distance of ~ 1000 km. Amplitude perturbations for the same scenario can be several tens of percent. With decreasing
5 frequency, amplitude perturbations decrease rapidly, but traveltime perturbations remain at approximately the same level. This indicates that the observed traveltime variations are a finite-frequency effect, i.e. a local change of amplitudes that manifests itself as a time shift, when the time shift is measured by cross-correlation.

Both amplitude and traveltime variations increase with increasing epicentral distance. This indicates that density does not only have a local effect, which is an essential prerequisite for the applicability of tomographic methods to constrain 3D density
10 in the crust. Waveform perturbations clearly increase with increasing medium complexity. They are practically negligible in transmission mode, i.e. when the correlation length of the medium heterogeneities is much larger than the wavelength. However, when the correlation length approaches the wavelength, density-induced waveform perturbations can be observed easily. Recent regional-scale full-waveform inversions operate in a regime where resolved heterogeneities have characteristic sizes comparable to the wavelength (e.g. Tape *et al.*, 2010; Fichtner *et al.*, 2013).

15 Our most important finding is that waveform perturbations induced by realistic crustal density variations can certainly be observed in modern, high-quality regional seismic data. While traveltime differences of typically less than 1 s will often be small compared to traveltime differences caused by velocity heterogeneities, amplitude variations of more than 10 % are comparable with those induced by 3D velocity structure and attenuation. This implies, on the one hand, that density structure may to some extend be constrained in future full-waveform inversions. On the other hand it suggests that current full-waveform
20 inversions that use amplitude information may be biased due to the neglect of 3D variations in density.

Appendix A: Random model generation

We generate random media with the Fourier method, widely used in seismological research (e.g. Frankel & Clayton, 1986; Frankel, 1989; Igel & Gudmundsson, 1997; Klimeš, 2002; Jahnke *et al.*, 2008), and recently extended to non-stationary and anisotropic media by Meschede & Romanowicz (2015). For this, we generate a random, uniformly distributed phase spectrum
25 $\varphi(\mathbf{k})$ between $-\pi$ and π, with $\mathbf{k}$ being the 3D wavenumber. The random spectrum $e^{i\,\varphi(\mathbf{k})}$ is then modulated by a positive, real-valued filter $f(\mathbf{k})$ to yield the wavenumber-domain random model

$$m(\mathbf{k}) = f(\mathbf{k})\,e^{i\,\varphi(\mathbf{k})}. \tag{A1}$$

The filter $f(\mathbf{k})$ is designed such that it is flat below k_{max} and wavenumber components k_i above a given threshold $k_{i,\max} = 2\pi/\lambda_{i,\min}$ are excluded. Computing the inverse Fourier transform, yields the space-domain random model

30 $$m(\mathbf{x}) = \frac{1}{(2\pi)^3} \iiint m(\mathbf{k})\,e^{i\,\mathbf{k}\cdot\mathbf{x}}\,d\mathbf{k}. \tag{A2}$$

By design, the 3D field $m(\mathbf{x})$ only contains wavelengths above $\lambda_{i,\text{min}}$ in the i-direction. Finally, the random realisation $m(\mathbf{x})$ is appropriately scaled and assigned to a specific medium parameter, such as density, P- or S-velocity.

Author contributions. Agnieszka Plonka performed all 3D numerical wave propagation experiments. All three authors were involved in the design of the experiments, the interpretation of results and the manuscript writing.

5 *Acknowledgements.* The authors would like to thank Hanneke Paulssen, Ivan Pires de Vasconcelos and Jeannot Trampert for numerous interesting discussions, and two anonymous reviewers for their constructive comments. This research was supported by the Swiss National Supercomputing Center (CSCS) in the form of the GeoScale and CH1 projects, and by the Netherlands Organisation for Scientific Research (VIDI grant 864.11.008).

References

Aki, K. and Richards, P.: Quantitative Seismology., University Science Books., 2002.

Backus, G. E. and Gilbert, F.: The resolving power of gross Earth data, Geophys. J. Roy. Astr. Soc., 16, 169–205, 1968.

Backus, G. E. and Gilbert, F.: Uniqueness in the inversion of inaccurate gross Earth data, Phil. Trans. R. Soc. London, A, 266, 123–192, 1970.

Becker, T. W. and Boschi, L.: A comparison of tomographic and geodynamic mantle models, Geochem. Geophys. Geosys., 3, doi:10.129/2001GC000 168, 2002.

Bozdağ, E., Trampert, J., and Tromp, J.: Misfit functions for full waveform inversion based on instantaneous phase and envelope measurements, Geophys. J. Int., 185, 845–870, 2011.

Bunge, H.-P., Hagelberg, C. R., and Travis, B. J.: Mantle circulation models with variational data assimilation: Inferring past mantle flow and structure from plate motion histories and seismic tomography, Geophys. J. Int., 152, 280–301, 2003.

Chen, P., Zhao, L., and Jordan, T. H.: Full 3D tomography for the crustal structure of the Los Angeles region., Bull. Seismol. Soc. Am., 97, 1094–1120, 2007.

Cupillard, P., Delavaud, E., Burgos, G., Festa, G., Vilotte, J.-P., Capdeville, Y., and Montagner, J.-P.: RegSEM: a versatile code based on the spectral element method to compute seismic wave propagation at the regional scale, Geophys. J. Int., 188, 1203–1220, 2012.

Dahlen, F., Hung, S.-H., and Nolet, G.: Fréchet kernels for finite-frequency traveltimes – I. Theory, Geophys. J. Int., 141, 157–174, 2000.

Dahlen, F. A. and Tromp, J.: Theoretical Global Seismology, Princeton University Press. NJ, 1998.

Dalton, C. A., Ekström, G., and Dziewonski, A. M.: The global attenuation structure of the upper mantle, J. Geophys. Res., 113, doi:10.1029/2007JB005 429, 2008.

Dziewoński, A. M. and Anderson, D. L.: Preliminary reference Earth model, Phys. Earth Planet. Inter., 25, 297–356, 1981.

Dziewoński, A. M., Hager, B. H., and O'Connell, R. J.: Large-scale heterogeneities in the lower mantle, J. Geophys. Res., 82, 239–255, 1977.

Faccioli, E., Maggio, F., Quarteroni, A., and Tagliani, A.: Spectral-domain decomposition methods for the solution of acoustic and elastic wave equations, Geophysics, 61:4, 1160–1174, 1996.

Fichtner, A.: Full Seismic Waveform Modelling and Inversion., Springer, Heidelberg., 2010.

Fichtner, A. and Villaseñor, A.: Subduction and volcanism in the western Mediterranean - Constraints from full-waveform inversion, Earth Planet. Sci. Lett., p. in review, 2015.

Fichtner, A., Kennett, B. L. N., Igel, H., and Bunge, H.-P.: Theoretical background for continental- and global-scale full-waveform inversion in the time-frequency domain., Geophys. J. Int., 175, 665–685, 2008.

Fichtner, A., Kennett, B. L. N., Igel, H., and Bunge, H.-P.: Full seismic waveform tomography for upper-mantle structure in the Australasian region using adjoint methods., Geophys. J. Int., 179, 1703–1725, 2009a.

Fichtner, A., Kennett, B. L. N., Igel, H., and Bunge, H.-P.: Spectral-element simulation and inversion of seismic waves in a spherical section of the Earth., J. Num. An. Ind. Appl. Math., 4, 11–22, 2009b.

Fichtner, A., Saygin, E., Taymaz, T., Cupillard, P., Capdeville, Y., and Trampert, J.: The deep structure of the North Anatolian Fault Zone, Earth Planet. Sci. Lett., 373, 109–117, 2013a.

Fichtner, A., Trampert, J., Cupillard, P., Saygin, E., Taymaz, T., Capdeville, Y., and Villasenor, A.: Multi-scale full waveform inversion, Geophys. J. Int., 194, 534–556, 2013b.

Frankel, A.: A review of numerical experiments on seismic wave scattering, Pure Appl. Geophys., 4, 639–685, 1989.

Furumura, T. and Kennett, B. L. N.: Subduction zone guided waves and the heterogeneity structure of the subducted plate – intensity anomalies in northern Japan, J. Geophys. Res., 110, doi:10.129/2004JB003 486, 2005.

Gokhberg, A. and Fichtner, A.: Full-waveform inversion on heterogeneous HPC systems, Comp. Geosci., p. in review, 2015.

5   Groenenboom, J. and Sneider, R.: Attenuation, dispersion, and anisotropy by multiple scattering of transmitted waves through distributions of scatterers, J. Acoust. Soc. Am., 98, 3482, 1995.

Ishii, M. and Tromp, J.: Normal-mode and free-air gravity constraints on lateral variations in velocity and density of Earth's mantle, Science, 285, 1231–1236, 1999.

Ishii, M. and Tromp, J.: Even-degree lateral variations in the Earth's mantle constrained by free oscillations and the free-air gravity anomaly.,
10   Geophys. J. Int., 145, 77–96, 2001.

Ishii, M. and Tromp, J.: Constraining large-scale mantle heterogeneity using mantle and inner-core sensitive normal modes., Phys. Earth Planet. Inter., 146, 113–124, 2004.

Kennett, B. L. N.: The seismic wavefield I. - Introduction and theoretical development., Cambridge University Press., 2001.

Kennett, B. L. N. and Abdullah, A.: Seismic wave attenuation beneath the Australasian region, Austr. J. Earth Sci., 58, 285–295, 2011.

15   Kennett, B. L. N. and Furumura, T.: Stochastic waveguide in the lithosphere: Indonesian subduction zone to Australian craton, Geophys. J. Int., 172, 363–382, 2008.

Koelemeijer, P., Deuss, A., and Ritsema, J.: Density structure of Earth's lowermost mantle from Stoneley mode splitting observations, Nature Geoscience, p. In preparation, 2015.

Komatitsch, D. and Tromp, J.: Introduction to the spectral element method for three-dimensional seismic wave propagation, Geophys. J. Int.,
20   139, 806–822, 1999.

Komatitsch, D. and Vilotte, J. P.: The spectral element method: an effective tool to simulate the seismic response of 2D and 3D geological structures, Bull. Seism. Soc. Am., 88, 368–392, 1998.

Kristekova, M., Kristek, J., Moczo, P., and Day, S. M.: Misfit criteria for quantitative comparison of seismograms, Bull. Seis. Soc. Am., 96, 1836–1850, 2006.

25   Kuo, C. and Romanowicz, B.: On the resolution of density anomalies in the Earth's mantle using spectral fitting of normal mode data, Geophys. J. Int., 150, 162–179, 2002.

Liu, L. and Gurnis, M.: Simultaneous inversion of mantle properties and initial conditions using an adjoint of mantle convection, J. Geophys. Res., 113, doi:10.1029/2007JB005 594, 2008.

Maceira, M. and Ammon, C. J.: Joint inversion of surface wave velocity and gravity observations and its application to central Asian basins
30   shear velocity structure, J. Geophys. Res., 114, doi:1029/2007JB005 157, 2009.

Mosca, I., Cobden, L., Deuss, A., Ritsema, J., and Trampert, J.: Seismic and mineralogical structures of the lower mantle from probabilistic tomography, J. Geophys. Res., 117, doi:10.1029/2011JB008 851, 2012.

Nataf, H. C. and Ricard, Y.: 3SMAC: an a priori tomographic model of the upper mantle based on geophysical modelling, Phys. Earth. Planet. Int., 95, 101–122, 1996.

35   Peter, D., Komatitsch, D., Luo, Y., Martin, R., Le Goff, N., Casarotti, E., Le Loher, P., Magnoni, F., Liu, Q., Blitz, C., Nissen-Meyer, T., Basini, P., and Tromp, J.: Forward and adjoint simulations of seismic wave propagation on fully unstructured hexahedral meshes, Geophys. J. Int., 186, 721–739, 2011.

Resovsky, J. and Ritzwoller, M.: Regularisation uncertainty in density models estimated from normal mode data, Geophys. Res. Lett., 26, 2319–2322, 1999.

Rickers, F., Fichtner, A., and Trampert, J.: Imaging mantle plumes with instantaneous phase measurements of diffracted waves, Geophys. J. Int., 190, 650–664, 2012.

5 Rickers, F., Fichtner, A., and Trampert, J.: The Iceland - Jan Mayen plume system and its impact on mantle dynamics in the North Atlantic region: Evidence from full-waveform inversion, Earth Planet. Sci. Lett., 367, 39–51, 2013.

Romanowicz, B.: A global tomographic model of shear attenuation in the upper mantle, J. Geophys. Res., 100, 12 375–12 394, 1995.

Romanowicz, B.: Can we resolve 3D density heterogeneity in the lower mantle?, Geophys. Res. Lett., 28, 1107–1110, 2001.

Selby, N. D. and Woodhouse, J. H.: The Q structure of the upper mantle: Constraints from Rayleigh wave amplitudes, J. Geophys. Res., 107,
10 doi:10.1029/2001JB000 257, 2002.

Shapiro, N. M., Campillo, M., Stehly, L., and Ritzwoller, M.: High resolution surface wave tomography from ambient seismic noise, Science, 307, 1615–1618, 2005.

Sieminski, A., Trampert, J., and Tromp, J.: Principal component analysis of anisotropic finite-frequency kernels, Geophys. J. Int., 179, 1186–1198, 2009.

15 Simmons, N. A., Forte, A. M., Boschi, L., and Grand, S. P.: GyPSuM: A joint tomography model of mantle density and seismic wave speeds, J. Geophys. Res., 115, doi:10.1029/2010JB007 631, 2010.

Takeuchi, H. and Saito, M.: Seismic surface waves, in: Methods in Computational Physics, editor B. A. Bolt, 11, 217–295, 1972.

Tape, C., Liu, Q., Maggi, A., and Tromp, J.: Seismic tomography of the southern California crust based upon spectral-element and adjoint methods., Geophys. J. Int., 180, 433–462, 2010.

20 Tarantola, A.: A strategy for nonlinear elastic inversion of seismic reflection data., Geophysics, 51, 1893–1903, 1986.

Tondi, R., de Franco, R., and Barzaghi, R.: Sequential inversion of refraction and wide-angle reflection traveltimes and gravity data for two-dimensional velocity structures, Geophys. J. Int., 141, 679–698, 2000.

Tondi, R., Achauer, U., Landes, M., Davi, R., and Besutiu, L.: Unveiling seismic and density structure beneath the Vrancea seismogenic zone, Romania, J. Geophys. Res., 141, doi:10.1029/2008JB005 992, 2009.

25 Trampert, J. and Fichtner, A.: Global imaging of the Earth's deep interior: seismic constraints on (an)isotropy, density and attenuation, in: Physics and Chemistry of the deep Earth, edited by Karato, S., Wiley-Blackwell, 2013.

Trampert, J., Deschamps, F., Resovsky, J., and Yuen, D.: Probabilistic tomography maps chemical heterogeneities throughout the lower mantle., Science, 306, 853–856, 2004.

Tromp, J., Tape, C., and Liu, Q.: Seismic tomography, adjoint methods, time reversal and banana-doughnut kernels, Geophys. J. Int., 160,
30 195–216, 2005.

van Leeuwen, T. and Mulder, W. A.: A correlation-based misfit criterion for wave-equation traveltime tomography, Geophys. J. Int., 182, 1383–1394, 2010.

Woodhouse, J. H.: The Calculation of Eigenfrequencies and Eigenfunctions of the Free Oscillations of the Earth and the Sun, in: Seismological algorithms, edited by Doornbos, D. J., pp. 321–370, Academic Press, New York, 1988.

35 Wu, R. and Aki, K.: Scattering characteristics of elastic waves by an elastic heterogeneity., Geophysics, 50, 582–595, 1985.

Yanhua O Yuan, F. J. S. and Bozdag, E.: Multiscale Adjoint Waveform Tomography for Surface and Body Waves, Geophysics, 80, 281–302, 2015.

Zhu, H., Bozdağ, E., and Tromp, J.: Seismic structure of the European upper mantle based on adjoint tomography, Geophys. J. Int., 201, 18–52, 2015.

References

Aki, K. & Richards, P., 2002. *Quantitative Seismology*. University Science Books.

Anderson, D. L., Schreiber, E., Lieberman, R. C. & Soga, N., 1968. Some elastic constant data on minerals relevant to geophysics. *Rev. Geophys. Space Phys.*, **6**, 491–524.

Backus, G. E. & Gilbert, F., 1968. The resolving power of gross Earth data. *Geophys. J. Roy. Astr. Soc.*, **16**, 169–205.

Backus, G. E. & Gilbert, F., 1970. Uniqueness in the inversion of inaccurate gross Earth data. *Phil. Trans. R. Soc. London, A*, **266**, 123–192.

Becker, T. W. & Boschi, L., 2002. A comparison of tomographic and geodynamic mantle models. *Geochem. Geophys. Geosys.*, **3**, doi:10.129/2001GC000168.

Bernauer, M., Fichtner, A. & Igel, H., 2014. Optimal observables for multi-parameter seismic tomography. *Geophys. J. Int.*, **198**, 1241–1254.

Bozdağ, E., Trampert, J. & Tromp, J., 2011. Misfit functions for full waveform inversion based on instantaneous phase and envelope measurements. *Geophys. J. Int.*, **185**, 845–870.

Brocher, T. M., 2005. Empirical relations between elastic wavespeeds and density in the Earth's crust. *Bull. Seis. Soc. Am. 95*(6), 2081–2092.

Bunge, H.-P., Hagelberg, C. R. & Travis, B. J., 2003. Mantle circulation models with variational data assimilation: Inferring past mantle flow and structure from plate motion histories and seismic tomography. *Geophys. J. Int.*, **152**, 280–301.

Cerveny, V., 2001. *Seismic ray theory*. Cambridge University Press.

Chen, P., Zhao, L. & Jordan, T. H., 2007. Full 3D tomography for the crustal structure of the Los Angeles region. *Bull. Seismol. Soc. Am.*, **97**, 1094–1120.

Chen, M., Niu, F., Liu, Q., Tromp, J. & Zheng, X., 2015. Multi-parameter adjoint tomography of the crust and upper mantle beneath East Asia - Part I: Model construction and comparisons. *J. Geophys. Res.*, **120**, 1762–1786.

Christensen, N. I. & Mooney, W. D., 1995. Seismic velocity structure and composition of the continental crust: a global view. *J. Geophys. Res.*, **1000**, 9761–9788.

Cupillard *et al.* 2012 (@)(@)Cupillard₂012*Cupillard, P., Delavaud, E., Burgos, G., Festa, G., Vilotte, J. − P., Capdeville, Y.& Montagner, J. − 1*

Dahlen, F., Hung, S.-H. & Nolet, G., 2000. Fréchet kernels for finite-frequency traveltimes – I. Theory. *Geophys. J. Int.*, **141**, 157–174.

Dahlen, F. A. & Tromp, J., 1998. *Theoretical Global Seismology*. Princeton University Press. NJ.

Dalton, C. A., Ekström, G. & Dziewonski, A. M., 2008. The global attenuation structure of the upper mantle. *J. Geophys. Res.*, **113**, doi:10.1029/2007JB005429.

Dziewoński, A. M., Hager, B. H. & O'Connell, R. J., 1977. Large-scale heterogeneities in the lower mantle. *J. Geophys. Res.*, **82**, 239–255.

Dziewoński, A. M. & Anderson, D. L., 1981. Preliminary reference Earth model. *Phys. Earth Planet. Inter.*, **25**, 297–356.

El Moudnib, L., Villaseñor, A., Harnafi, M., Gallart, J., Pazos, A., Serrano, I., nd J. A. Pulgar, D. C., Ibarra, P., Himmi, M. M. & Chourak, M., 2015. Crustal structure of the Betic–Rif system, western Mediterranean, from local earthquake tomography. *Tectonophysics*, **643**, 94–105.

Faccioli, E., Maggio, F., Quarteroni, A. & Tagliani, A., 1996. Spectral-domain decomposition methods for the solution of acoustic and elastic wave equations. *Geophysics*, **61:4**, 1160–1174.

Fichtner, A., Kennett, B. L. N., Igel, H. & Bunge, H.-P., 2008. Theoretical background for continental- and global-scale full-waveform inversion in the time-frequency domain. *Geophys. J. Int.*, **175**, 665–685.

Fichtner, A., Kennett, B. L. N., Igel, H. & Bunge, H.-P., 2009. Full seismic waveform tomography for upper-mantle structure in the Australasian region using adjoint methods. *Geophys. J. Int.*, **179**, 1703–1725.

Fichtner, A., Kennett, B. L. N., Igel, H. & Bunge, H.-P., 2009. Spectral-element simulation and inversion of seismic waves in a spherical section of the Earth. *J. Num. An. Ind. Appl. Math.*, **4**, 11–22.

Fichtner, A., 2010. *Full Seismic Waveform Modelling and Inversion.* Springer, Heidelberg.

Fichtner, A., Saygin, E., Taymaz, T., Cupillard, P., Capdeville, Y. & Trampert, J., 2013. The deep structure of the North Anatolian Fault Zone. *Earth Planet. Sci. Lett.*, **373**, 109–117.

Fichtner, A. & Villaseñor, A., 2015. Crust and upper mantle of the western Mediterranean – Constraints from full-waveform inversion. *Earth Planet. Sci. Lett.*, **428**, 52–62.

Fichtner, A., Trampert, J., Cupillard, P., Saygin, E., Taymaz, T., Capdeville, Y. & Villasenor, A., 2013. Multi-scale full waveform inversion. *Geophys. J. Int.*, **194**, 534–556.

Frankel, A., 1989. A review of numerical experiments on seismic wave scattering. *Pure Appl. Geophys.*, **4**, 639–685.

Frankel, A. & Clayton, R., 1986. Finite-difference simulations of seismic scattering: implications for the propagation of of short period seismic waves in the crust and models of crustal heterogeneity. *J. Geophys. Res.*, **91**, 6465–6489.

Furumura, T. & Kennett, B. L. N., 2005. Subduction zone guided waves and the heterogeneity structure of the subducted plate – intensity anomalies in northern Japan. *J. Geophys. Res.*, **110**, doi:10.129/2004JB003486.

Gaite, B., Villaseñor, A., Iglesias, A., Herraiz, M. & Jiménez-Munt, I., 2015. A 3-D shear velocity model of the southern North American and Caribbean plates from ambient noise and earthquake tomography. *Solid Earth.*, **6**, 271–284.

Gardner, G. H. F., Gardner, L. W. & Gregory, A. R., 1974. Formation velocity and density—the diagnostic basics for stratigraphic traps. *Geophysics*, **39**, 770–780.

Gokhberg, A. & Fichtner, A., 2016. Full-waveform inversion on heterogeneous HPC systems. *Comp. Geosci.*, doi: 10.1016/j.cageo.2015.12.013.

Haberland, C. & Rietbrock, A., 2001. Attenuation tomography in the western central Andes: A detailed insight into the structure of a magmatic arc. *J. Geophys. Res.*, **106**, 11151–11167.

Igel, H. & Gudmundsson, O., 1997. Frequency-dependent effects on travel times and waveforms of long-period S and SS waves. *Phys. Earth. Planet. Int.*, **104**, 229–246.

Ishii, M. & Tromp, J., 1999. Normal-mode and free-air gravity constraints on lateral variations in velocity and density of Earth's mantle. *Science*, **285**, 1231–1236.

Ishii, M. & Tromp, J., 2001. Even-degree lateral variations in the Earth's mantle constrained by free oscillations and the free-air gravity anomaly. *Geophys. J. Int.*, **145**, 77–96.

Ishii, M. & Tromp, J., 2004. Constraining large-scale mantle heterogeneity using mantle and inner-core sensitive normal modes. *Phys. Earth Planet. Inter.*, **146**, 113–124.

Jahnke, G., Thorne, M. S., Cochard, A. & Igel, H., 2008. Global SH-wave propagation using a parallel axisymmetric spherical finite-difference scheme: application to whole-mantle scattering. *Geophys. J. Int.*, **173**, 815–826.

Jordan, T. H., 1975. The continental tectosphere. *Rev. Geophys.*, **13**, 1–12.

Jordan, T. H., 1978. Composition and development of the continental tectosphere. *Nature*, **274**, 544–548.

Kennett, B. L. N., 2001. *The seismic wavefield I. - Introduction and theoretical development.* Cambridge University Press.

Kennett, B. L. N. & Furumura, T., 2008. Stochastic waveguide in the lithosphere: Indonesian subduction zone to Australian craton. *Geophys. J. Int.*, **172**, 363–382.

Kennett, B. L. N. & Bunge, H.-P., 2008. *Geophysical Continua.* Cambridge University Press.

Kennett, B. L. N. & Abdullah, A., 2011. Seismic wave attenuation beneath the Australasian region. *Austr. J. Earth Sci.*, **58**, 285–295.

Klimeš, L., 2002. Correlation functions of random media. *Pure appl. Geophys.*, **159**, 1811–1831.

Koelemeijer, P., Deuss, A. & Ritsema, J., 2015. Density structure of earth's lowermost mantle from stoneley mode splitting observations. *Nature ~~Geoscience~~Communications*, ~~In preparation~~Under review.

Komatitsch, D. & Tromp, J., 1999. Introduction to the spectral element method for three-dimensional seismic wave propagation. *Geophys. J. Int.*, **139**, 806–822.

Komatitsch, D. & Vilotte, J. P., 1998. The spectral element method: an effective tool to simulate the seismic response of 2D and 3D geological structures. *Bull. Seism. Soc. Am.*, **88**, 368–392.

Kristekova, M., Kristek, J. & Moczo, P., 2009. Time.frequency misfit and goodness-of-fit criteria for quantitative comparison of time signals. *Geophys. J. Int.*, **178**, 813–825.

Kristekova, M., Kristek, J., Moczo, P. & Day, S. M., 2006. Misfit criteria for quantitative comparison of seismograms. *Bull. Seis. Soc. Am.*, **96**, 1836–1850.

Kuo, C. & Romanowicz, B., 2002. On the resolution of density anomalies in the Earth's mantle using spectral fitting of normal mode data. *Geophys. J. Int.*, **150**, 162–179.

Lin, F.-C. & Tsai, B. S. V. C., 2012. Joint inversion of Rayleigh wave phase velocity and ellipticity using USArray: Constraining velocity and density structure in the upper crust. *Geophy Res. Lett.*, **39**, doi:10.1029/2012GL052196.

Lin, F.-C., Tsai, V. C. & Ritzwoller, M. H., 2012. The local amplification of surface waves: A new observable to constrain elastic velocities, density, and anelastic attenuation. *J. Geophys. Res.*, **117**, doi:10.1029/2012JB009208.

Liu, L. & Gurnis, M., 2008. Simultaneous inversion of mantle properties and initial conditions using an adjoint of mantle convection. *J. Geophys. Res.*, **113**, doi:10.1029/2007JB005594.

Ludwig, W. J., Nafe, J. E. & Drake, C. L., 1970. Seismic refraction. In A. E. Maxwell (Ed.), *The Sea*. Wiley-Interscience, New York.

Maceira, M. & Ammon, C. J., 2009. Joint inversion of surface wave velocity and gravity observations and its application to central asian basins shear velocity structure. *J. Geophys. Res.*, **114**, doi:1029/2007JB005157.

Marquering, H., Dahlen, F. A. & Nolet, G., 1999. Three-dimensional sensitivity kernels for finite-frequency traveltimes: the banana-doughnut paradox. *Geophys. J. Int.*, **137**, 805–815.

Meschede, M. & Romanowicz, B., 2015. Non-stationary spherical random media and their effect on long-period mantle waves. *Geophys. J. Int.*, **203**, 1605–1625.

Mitchell, J. B., 1995. Anelastic structure and evolution of the continental crust and upper mantle from seismic surface wave attenuation. *Rev. Geophys.*, **33**, 441–462.

Mosca, I., Cobden, L., Deuss, A., Ritsema, J. & Trampert, J., 2012. Seismic and mineralogical structures of the lower mantle from probabilistic tomography. *J. Geophys. Res.*, **117**, doi:10.1029/2011JB008851.

Nataf, H. C. & Ricard, Y., 1996. 3SMAC: an a priori tomographic model of the upper mantle based on geophysical modelling. *Phys. Earth. Planet. Int.*, **95**, 101–122.

Peter, D., Komatitsch, D., Luo, Y., Martin, R., Le Goff, N., Casarotti, E., Le Loher, P., Magnoni, F., Liu, Q., Blitz, C., Nissen-Meyer, T., Basini, P. & Tromp, J., 2011. Forward and adjoint simulations of seismic wave propagation on fully unstructured hexahedral meshes. *Geophys. J. Int.*, **186**, 721–739.

Resovsky, J. & Ritzwoller, M., 1999. Regularisation uncertainty in density models estimated from normal mode data. *Geophys. Res. Lett.*, **26**, 2319–2322.

Resovsky, J. & Trampert, J., 2002. Reliable mantle density error bars: an application of the Neighbourhood Algorithm to normal-mode and surface wave data. *Geophys. J. Int. 150*(3), 665–672.

Richards, M. & Lithgow-Bertelloni, C., 1993. A geodynamic model of mantle density heterogeneity. *Journal of Geophysical Research 98*(B12), 21–895.

5   Rickers, F., Fichtner, A. & Trampert, J., 2012. Imaging mantle plumes with instantaneous phase measurements of diffracted waves. *Geophys. J. Int.*, **190**, 650–664.

Rickers, F., Fichtner, A. & Trampert, J., 2013. The Iceland - Jan Mayen plume system and its impact on mantle dynamics in the North Atlantic region: Evidence from full-waveform inversion. *Earth Planet. Sci. Lett.*, **367**, 39–51.

Romanowicz, B., 1995. A global tomographic model of shear attenuation in the upper mantle. *J. Geophys. Res.*, **100**, 12375–12394.

10   Romanowicz, B., 2001. Can we resolve 3D density heterogeneity in the lower mantle? *Geophys. Res. Lett.*, **28**, 1107–1110.

Romanowicz, B. & Mitchell, B. J., 2007. Deep Earth structure - *Q* of the Earth from Crust to Core. In G. Schubert (Ed.), *Treatise on Geophysics*, pp. 731–774. Elsevier.

Selby, N. D. & Woodhouse, J. H., 2002. The Q structure of the upper mantle: Constraints from Rayleigh wave amplitudes. *J. Geophys. Res.*, **107**, doi:10.1029/2001JB000257.

15   Shapiro, N. M., Campillo, M., Stehly, L. & Ritzwoller, M., 2005. High resolution surface wave tomography from ambient seismic noise. *Science*, **307**, 1615–1618.

Sieminski, A., Trampert, J. & Tromp, J., 2009. Principal component analysis of anisotropic finite-frequency kernels. *Geophys. J. Int.*, **179**, 1186–1198.

Simmons, N. A., Forte, A. M., Boschi, L. & Grand, S. P., 2010. GyPSuM: A joint tomography model of mantle density and seismic wave

20   speeds. *J. Geophys. Res.*, **115**, doi:10.1029/2010JB007631.

Tanimoto, T., 1991. Waveform inversion for three-dimensional density and S wave structure. *J. Geophys. Res.*, **96**, 8167–8189.

Takeuchi, H. & Saito, M., 1972. Seismic surface waves. *in: Methods in Computational Physics, editor B. A. Bolt*, **11**, 217–295.

Tape, C., Liu, Q., Maggi, A. & Tromp, J., 2010. Seismic tomography of the southern California crust based upon spectral-element and adjoint methods. *Geophys. J. Int.*, **180**, 433–462.

25   Tarantola, A., 1986. A strategy for nonlinear elastic inversion of seismic reflection data. *Geophysics*, **51**, 1893–1903.

Tondi, R., Achauer, U., Landes, M., Davi, R. & Besutiu, L., 2009. Unveiling seismic and density structure beneath the Vrancea seismogenic zone, Romania. *J. Geophys. Res.*, **141**, doi:10.1029/2008JB005992.

Tondi, R., de Franco, R. & Barzaghi, R., 2000. Sequential inversion of refraction and wide-angle reflection traveltimes and gravity data for two-dimensional velocity structures. *Geophys. J. Int.*, **141**, 679–698.

30   Tong, J., Dahlen, F. A., Nolet, G. & Marquering, H., 1998. Diffraction effects upon finite-frequency travel times: A simple 2-D example. *Geophys. Res. Lett.*, **25**, 1983–1986.

Trampert, J., Deschamps, F., Resovsky, J. & Yuen, D., 2004. Probabilistic tomography maps chemical heterogeneities throughout the lower mantle. *Science*, **306**, 853–856.

Trampert, J. & Fichtner, A., 2013. Global imaging of the Earth's deep interior: seismic constraints on (an)isotropy, density and attenuation.

35   In S. Karato (Ed.), *Physics and Chemistry of the deep Earth*. Wiley-Blackwell.

Tromp, J., Tape, C. & Liu, Q., 2005. Seismic tomography, adjoint methods, time reversal and banana-doughnut kernels. *Geophys. J. Int.*, **160**, 195–216.

Turcotte, D. L. & Schubert, G., 2014. *Geodynamics*. Cambridge University Press.

van Leeuwen, T. & Mulder, W. A., 2010. A correlation-based misfit criterion for wave-equation traveltime tomography. *Geophys. J. Int.*, **182**, 1383–1394.

Warners-Ruckstuhl, K. N., Govers, R. & Wortel, R., 2012. Lithosphere–mantle coupling and the dynamics of the Eurasian Plate. *Geophys. J. Int.*, **189**, 1253–1276.

5   Woodhouse, J. H., 1988. The calculation of eigenfrequencies and eigenfunctions of the free oscillations of the earth and the sun. In D. J. Doornbos (Ed.), *Seismological algorithms*, pp. 321–370. Academic Press, New York.

Woodhouse, J. H. & Deuss, A. F., 2007. Theory and Observations – Earth's Free Oscillations. In *Treatise on Geophysics*, pp. doi: 10.1016/B978–044452748–6.00002–X. Elsevier.

Wu, R. & Aki, K., 1985. Scattering characteristics of elastic waves by an elastic heterogeneity. *Geophysics*, **50**, 582–595.

10   Zhu, H., Bozdağ, E. & Tromp, J., 2015. Seismic structure of the European upper mantle based on adjoint tomography. *Geophys. J. Int.*, **201**, 18–52.
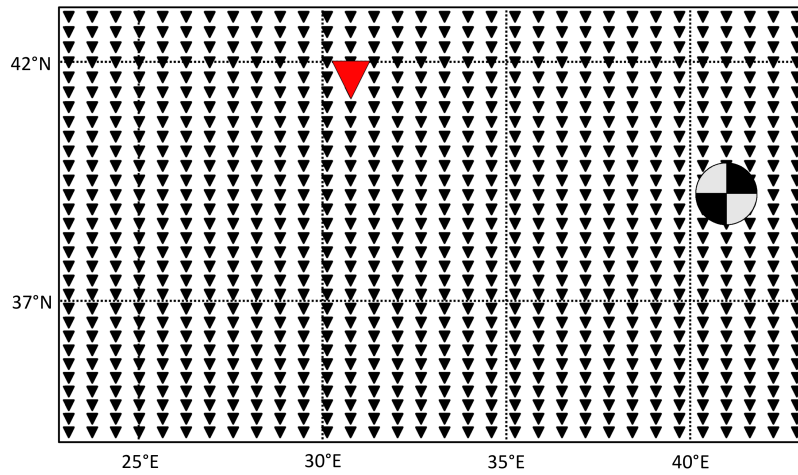
Figure 1. The grid of receivers (black triangles) on the surface of the computational domain. The source is located at 5 km depth, its location and orientation are indicated by the beachball plot. The receiver marked by a large red triangle and at an epicentral distance of 910 km is used for the examples presented in sections 3.1 and 3.2.
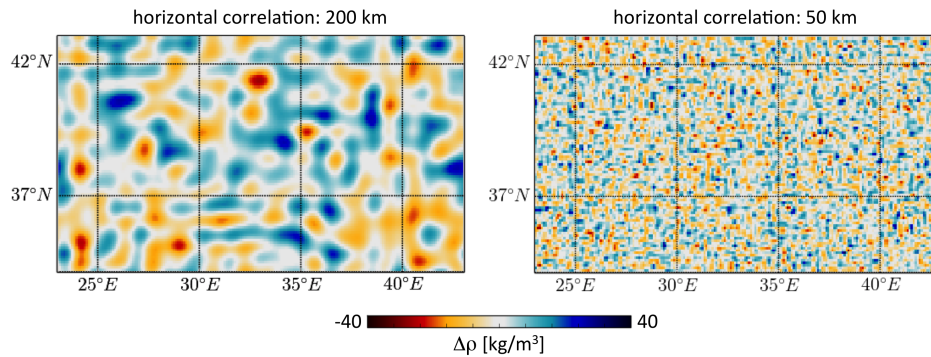
Figure 2. Realisations of random density variations. **Left**: 200 km lateral correlation length, 20 km vertical correlation length. **Right**: 50 km lateral correlation length, 10 km vertical correlation length.
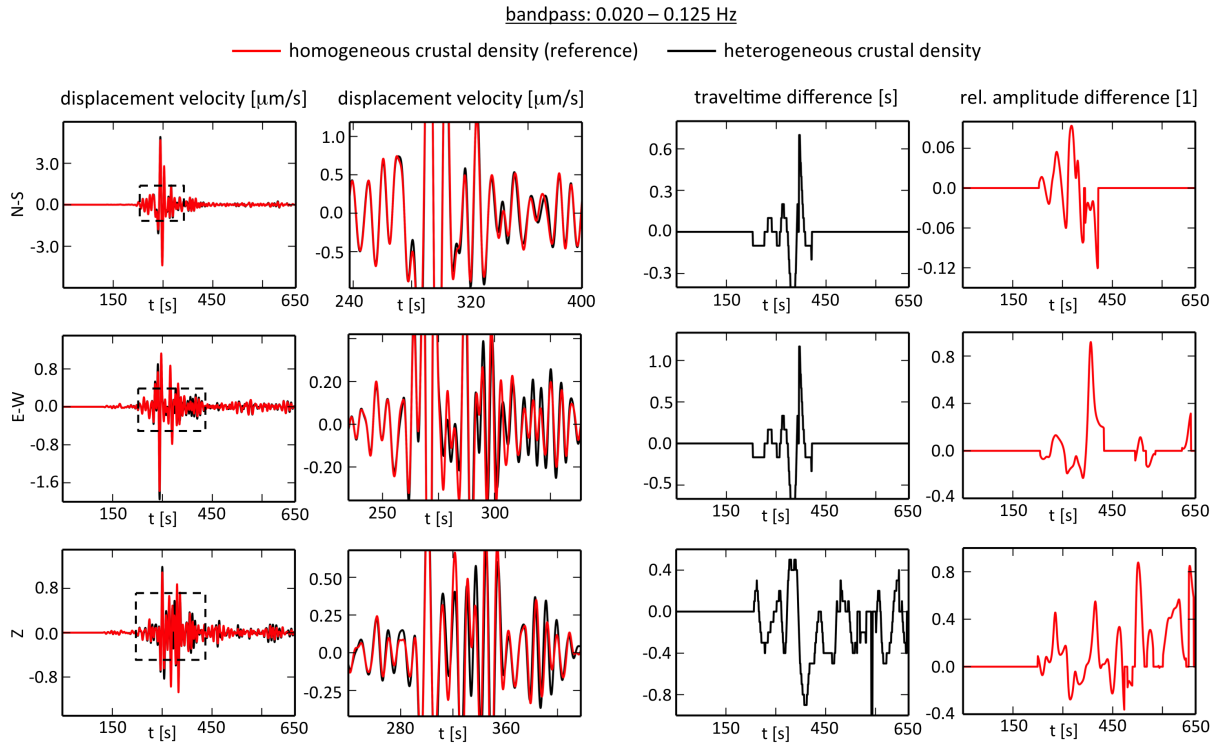
Figure 3. Comparison of synthetic seismograms for homogeneous and heterogeneous crustal densities in the broadest frequency band from 0.020 - 0.125 Hz (8 - 50 s). The receiver is located at an intermediate epicentral distance of 910 km, and is marked by a red tringle in figure 1. The correlation lengths of the heterogeneities in velocities and density are 200 km in the horizontal and 20 km in the vertical directions. The first column displays the seismograms on the N-S, E-W and Z components for the reference medium with homogeneous crustal density (red) and a medium with random heterogeneous crustal density (black). For better visibilty, a zoom into the interval indicated by the black-dashed box is shown in the second column. The third and fourth columns display the time-dependent traveltime and relative amplitude difference of the two sets of seismograms shown to the left. Extreme traveltime differences due to cycle skips are cropped to enhance visibility of physically meaningful traveltime variations.
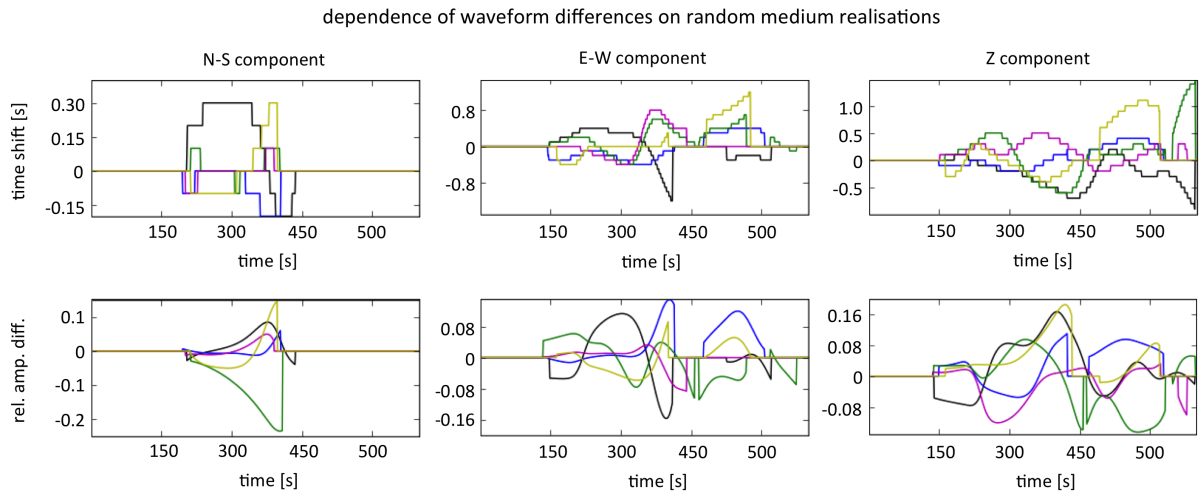
Figure 4. Component-wise time shifts and relative amplitude differences in the frequency band from $0.02 - 0.04$ Hz for five random media realisations.
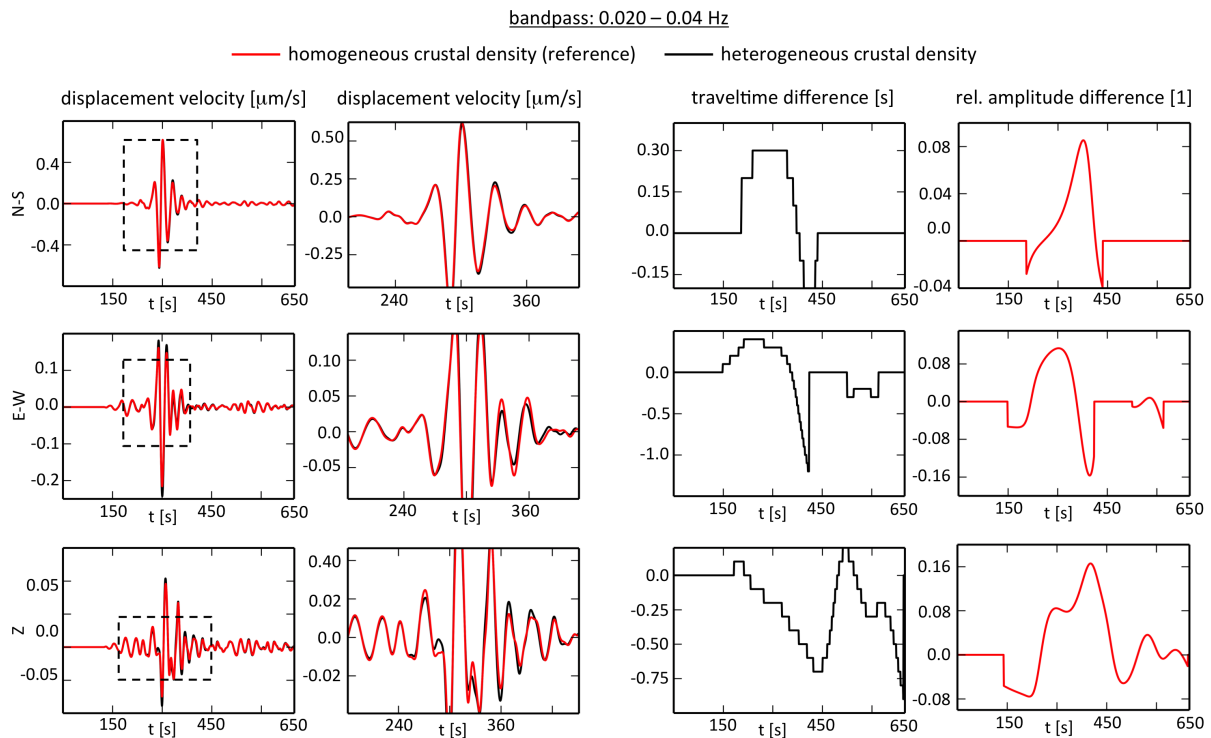
Figure 5. The same as in figure 3 but for the narrowest frequency band from $0.02 - 0.04$ Hz (25 - 50 s).
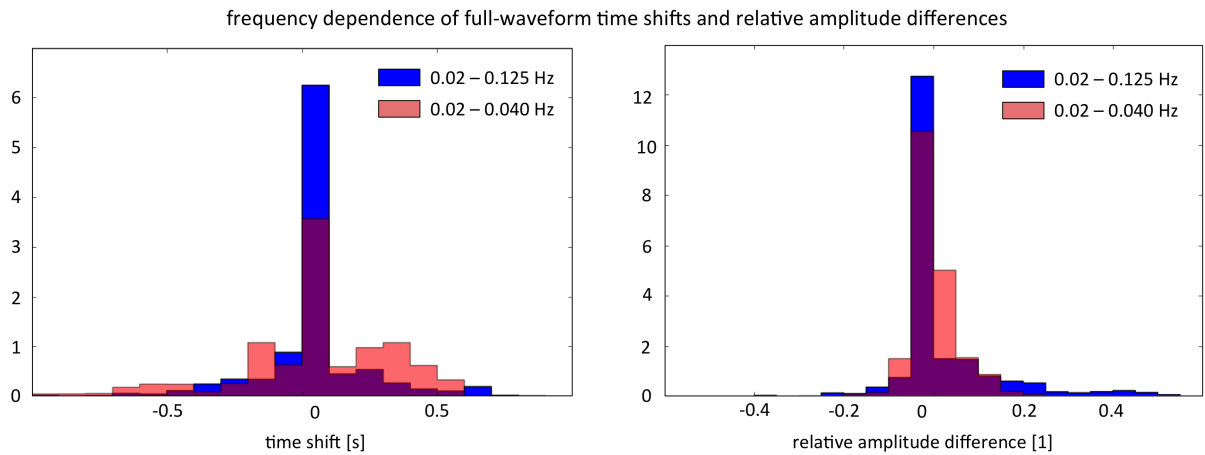
Figure 6. Normalised histograms of time shifts (left) and relative amplitude differences (right) averaged over five random media realisations with 200 km lateral and 20 km vertical correlation length. The lower frequency band from 0.02 - 0.04 Hz is shown in magenta, and the higher frequency and from 0.02 - 0.125 Hz in blue. Relative amplitude differences at higher frequencies (blue) have a visibly larger spread than at lower frequencies (magenta). The spreads of the time shift histograms are, however, comparable for both frequency bands. A summary of standard deviations in the histograms is provided in table 2.
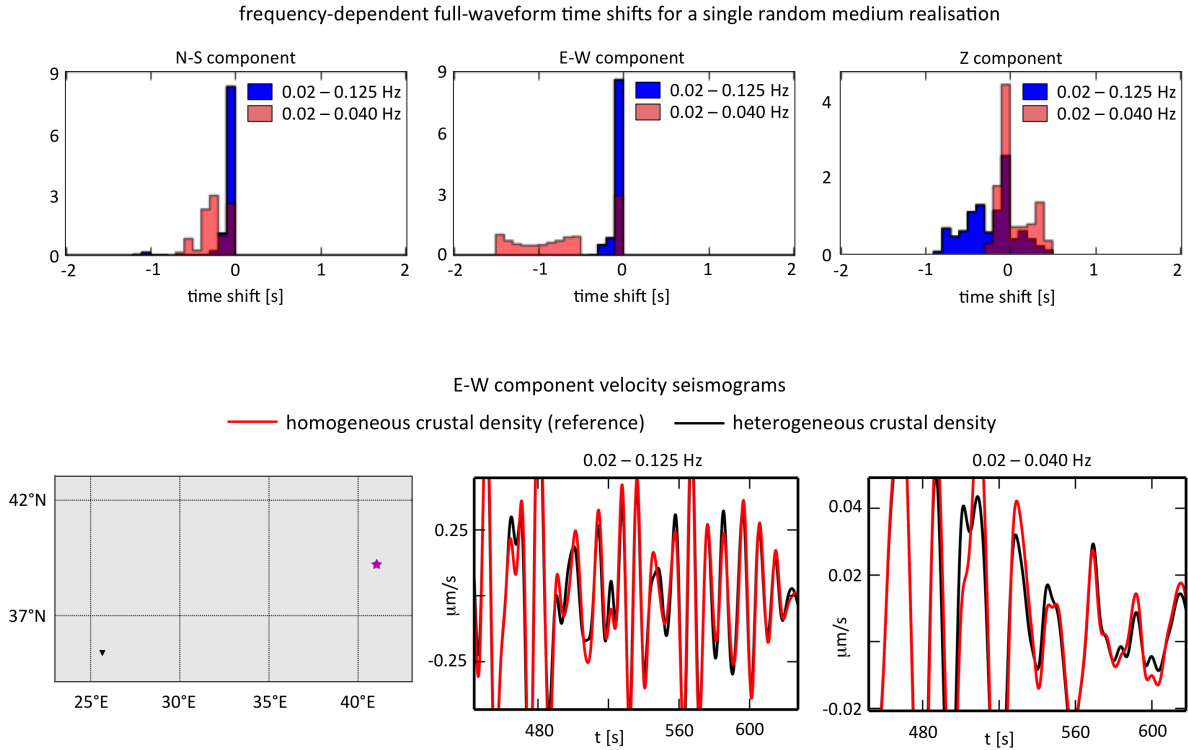
Figure 7. Top row: Normalised histograms of frequency-dependent time shifts for a single random medium realisation with 200 km lateral and 20 km vertical correlation length. The lower frequency band from 0.02 - 0.04 Hz is shown in magenta, and the higher frequency and from 0.02 - 0.125 Hz in blue. The three different components are plotted separately. The isolated tail of reduced time shifts for the lowest frequency band on the E-W component was observed for ~~three~~ two out of five random medium realisations, the average of which is shown in figure 6. **Bottom row**: Comparison of E-W component synthetic seismograms for the homogeneous reference crust (red) and the 3D heterogeneous crust (black) for the source-receiver geomtery shown in the left panel. In the lower frequency band from 0.02 - 0.04 Hz waves for the 3D heterogeneous crust arrive early by ~ 1 s, thus contributing to the negative time shift tail in the E-W component histogram shown above. For the higher frequency band from 0.02 - 0.125 Hz, a similar effect is not visible.
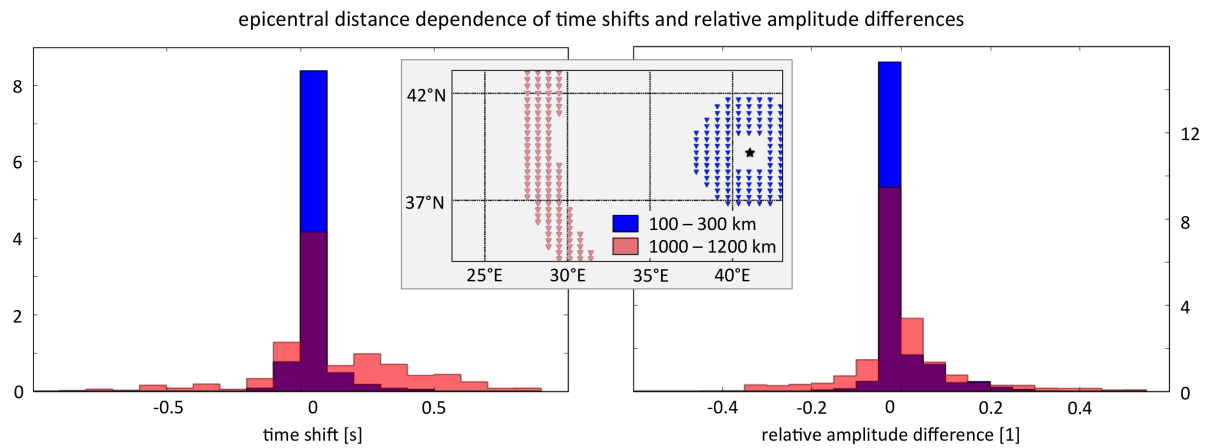
Figure 8. Normalised time shifts (left) and relative amplitude differences (right) for stations in two epicental distance ranges: 100 - 300 km (blue) and 1000 - 1200 km (magenta). The source-receiver configuration is shown in the inset. The frequency range is 0.02 - 0.125 Hz. The spread of both time shifts and relative amplitude differences increases with epicental distance, indicating that the observed waveform differences accumulate with increasing propagation distance instead of being a purely local effect.
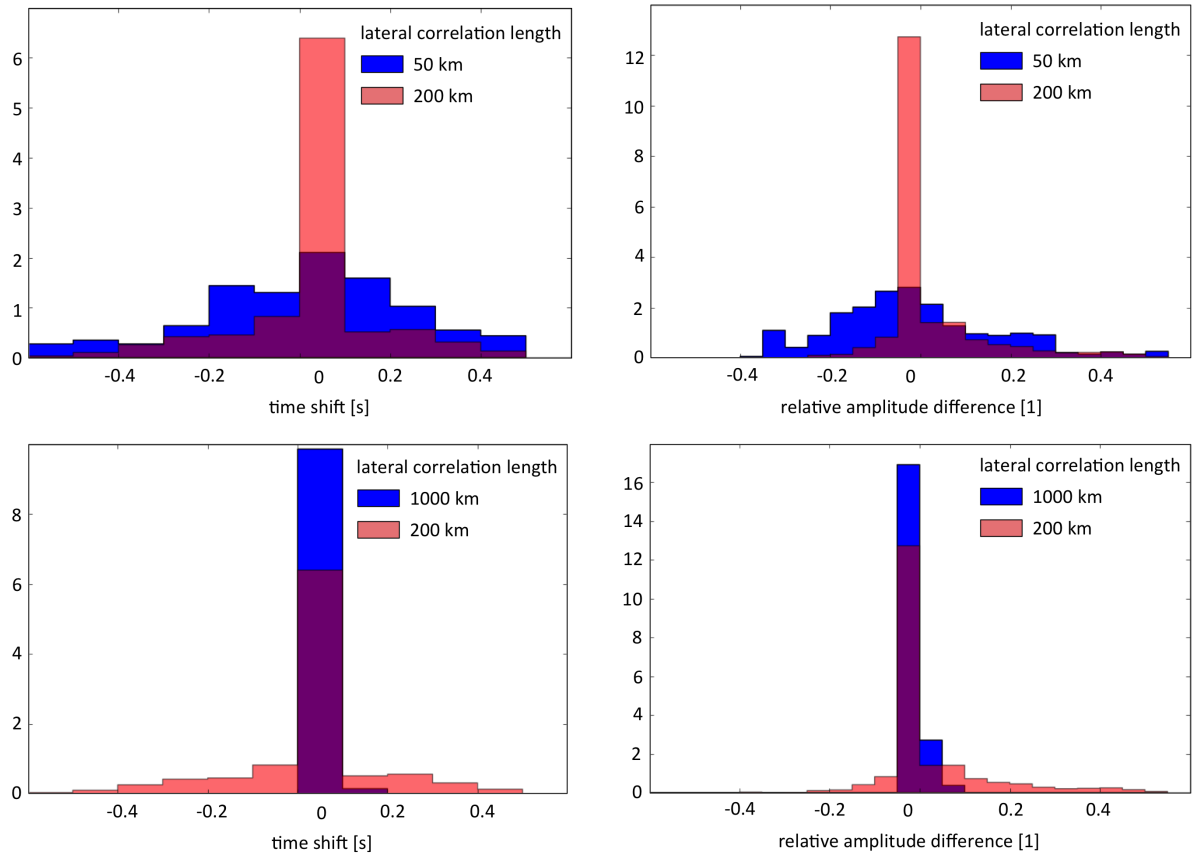
Figure 9. Histograms of time shifts (left) and relative amplitude differences (right) for a complex medium with 50 km lateral correlation length (top, blue) and a smooth medium with 1000 km lateral correlation length (bottom, blue). The medium with 200 km lateral correlation length, used in the previous sections, is used as reference and plotted in magenta. The frequency band is 0.02 - 0.125 Hz. Both time shifts and relative amplitude differences grow considerably with growing complexity of the medium.
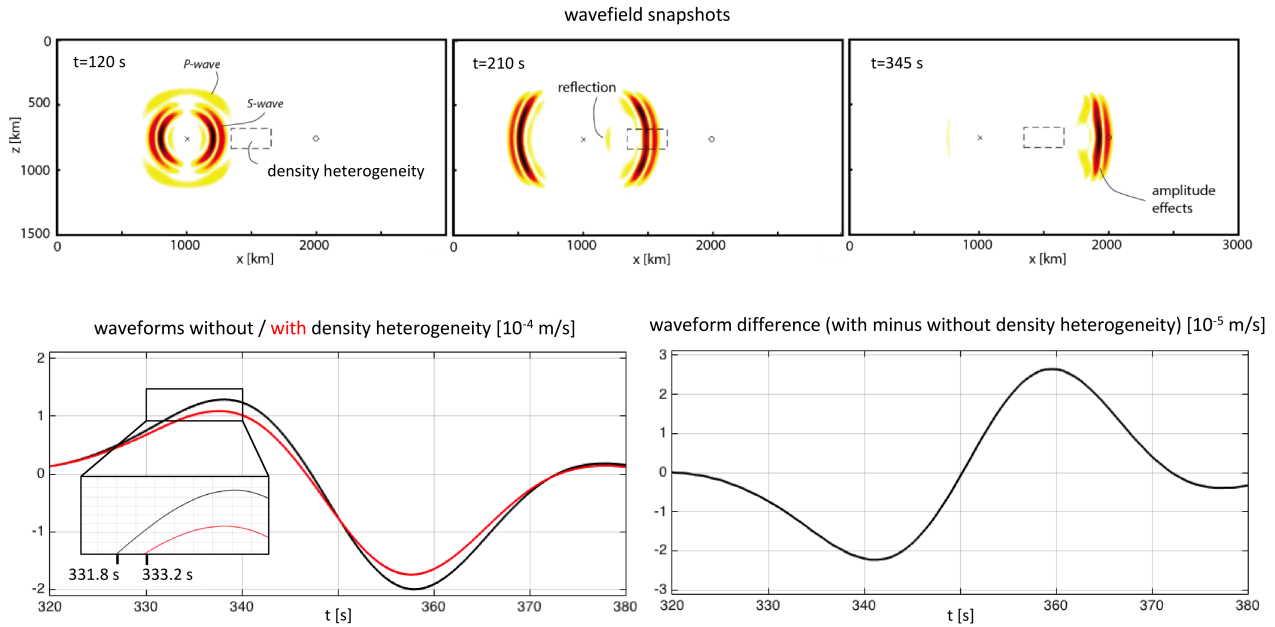
Figure 10. Illustration of finite-frequency traveltime shifts induced by a 38% density perturbation. **Top row**: Wavefield snapshots before, during and after the wavefront interacts with the density heterogeneity, ~~maked~~ marked by the dashed box. The interaction with the density heterogeneity causes reflections and amplitude changes of the direct wave. The onset of the wavefront, however, remains unaffected. **Bottom row**: Synthetic seismograms taken at the position of the black circle in the top-row snapshots. The actual onset time of the waveforms at around 320 s is identical for simulations with (red) and without (black) density heterogeneity. However, the waveform differences, plotted to the right, induce a cross-correlation time shift of ~ 1 s. Locally, e.g. around 332 s, the time shift reaches 1.4 s.
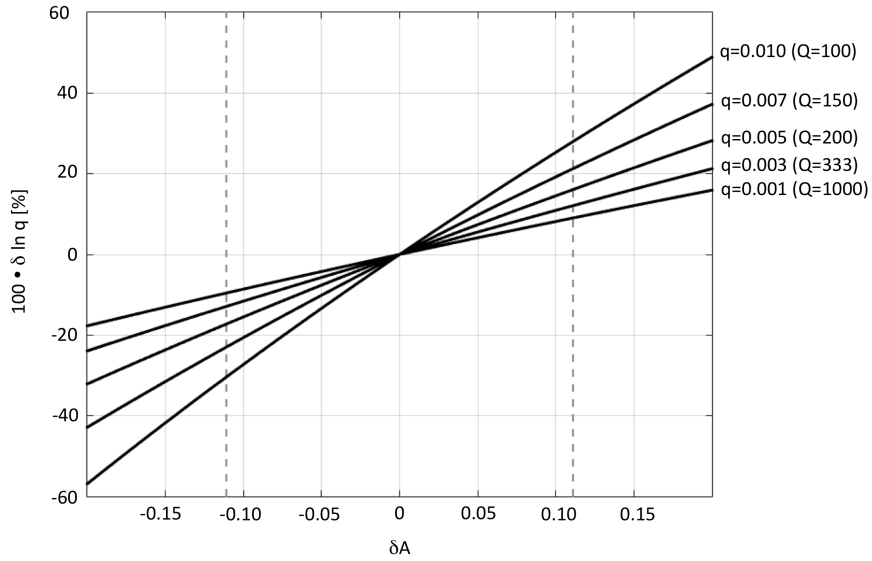
Figure 11. Fractional attenuation bias $\delta \ln q$ induced by 3D density variations as a function of the relative amplitude difference δA. Dashed lines indicate the standard deviation of δA for the setup that we used previously to study the effect of epicentral distance (epicentral distance: 1000 km, frequency band: 0.02 - 0.125 Hz, lateral correlation length: 200 km, vertical correlation length: 20 km; see section 3.3). The corresponding histrograms are shown in figure 8.

lateral correlation length [km]	vertical correlation length [km]
1000	100
200	20
50	10

Table 1. Lateral and vertical correlation lengths of random medium variations used to assess the influence of medium complexity.

frequency band	standard deviation of time shifts	standard deviation of relative amplitude differences
0.02 Hz - 0.04 Hz	0.38 s	0.07
0.02 Hz - 0.067 Hz	0.20s	0.06
0.02 Hz - 0.125 Hz	0.19 s	0.15

Table 2. Standard deviations of time shifts and relative amplitude differences as a function of frequency bandwidth.